Monthly Notices
of the
ROYAL ASTRONOMICAL SOCIETY

MNRAS **440,** 1856–1864 (2014)
Advance Access publication 2014 March 27

doi:10.1093/mnras/stu417

Type II Plateau supernovae as metallicity probes of the Universe

L. Dessart,[1]★† C. P. Gutierrez,[2] M. Hamuy,[2] D. J. Hillier,[3] T. Lanz,[1] J. P. Anderson,[2,4] G. Folatelli,[5] W. L. Freedman,[6] F. Ley,[2] N. Morrell,[7] S. E. Persson,[6] M. M. Phillips,[7] M. Stritzinger[8] and N. B. Suntzeff[9]

[1]*Laboratoire Lagrange, UMR7293, Université Nice Sophia-Antipolis, CNRS, Observatoire de la Côte dAzur, F-06300 Nice, France*
[2]*Departamento de Astronomía, Universidad de Chile, Casilla 36-D, Santiago, Chile*
[3]*Department of Physics and Astronomy and Pittsburgh Particle Physics, Astrophysics, and Cosmology Center (PITT PACC), University of Pittsburgh, 3941 O'Hara Street, Pittsburgh, PA 15260, USA*
[4]*European Southern Observatory, Alonso de Cordova 3107, Vitacura, Santiago, Chile*
[5]*Kavli Institute for the Physics and Mathematics of the Universe (WPI), Todai Institutes for Advanced Study, The University of Tokyo, Kashiwa 277-8583, Japan*
[6]*Observatories of the Carnegie Institution of Washington, 813 Santa Barbara St, Pasadena, CA 91101, USA*
[7]*Las Campanas Observatory, Carnegie Observatories, Casilla 601, La Serena, Chile*
[8]*Department of Physics and Astronomy, Aarhus University, Ny Munkegade 120, DK-8000 Aarhus C, Denmark*
[9]*George P. and Cynthia Woods Mitchell Institute for Fundamental Physics and Astronomy, Department of Physics and Astronomy, Texas A&M University, College Station, TX 77843, USA*

Accepted 2014 February 27. Received 2014 February 26; in original form 2014 January 25

ABSTRACT

We explore a method for metallicity determinations based on quantitative spectroscopy of Type II-Plateau supernovae (SNe II-P). For consistency, we first evolve a set of 15 $M_{\odot}$ main-sequence stars at 0.1, 0.4, 1, and 2 times the solar metallicity. At the onset of core collapse, we trigger a piston-driven explosion and model the resulting ejecta and radiation. Our theoretical models of such red supergiant star explosions at different metallicity show that synthetic spectra of SNe II-P possess optical signatures during the recombination phase that are sensitive to metallicity variations. This sensitivity can be quantified and the metallicity inferred from the strengths of metal-line absorptions. Furthermore, these signatures are not limited to O, but also include Na, Ca, Sc, Ti, or Fe. When compared to a sample of SNe II-P from the Carnegie SN Project and previous SN followup programmes, we find that most events lie at a metallicity between 0.4 and 2 times solar, with a marked scarcity of SN II-P events at small magellanic cloud metallicity. This most likely reflects the paucity of low-metallicity star-forming regions in the local Universe.

SNe II-P have high-plateau luminosities that make them observable spectroscopically at large distances. Because they exhibit signatures of diverse metal species, in the future they may offer a means to constrain the evolution of the composition (e.g. the O/Fe ratio) in the Universe out to a redshift of 1 and beyond.

Key words: radiative transfer – supernovae: general.

1 INTRODUCTION

Accurate metallicity measurements are desirable in numerous fields of astrophysics. For example, mapping the evolution of metallicity with redshift is instrumental for understanding how the composition of the Universe has evolved since big bang nucleosynthesis occurred. Stars (Burbidge et al. 1957) and their supernovae (SNe; Arnett 1996) are the primary nuclear nurseries and thus the metallicity evolution of the Universe allows us to look into the characteristics of the stars and SNe that drove that evolution (Nomoto, Kobayashi & Tominaga 2013). Accurate metallicity determinations are needed to interpret and to refine the mass–metallicity relation of galaxies (Tremonti et al. 2004), and to characterize the variation of metallicity with galactocentric radius in spiral galaxies, which is a probe of the star formation history and galaxy dynamics (Boissier & Prantzos 1999). An additional motivation is the need to better

★This paper includes data gathered with the 6.5 m Magellan Telescopes located at Las Campanas Observatory, Chile; and the Gemini Observatory, Cerro Pachon, Chile (Gemini Program GS-2008B−Q−56). Based on observations collected at the European Organization for Astronomical Research in the Southern hemisphere, Chile (ESO Programmes 076.A-0156, 078.D-0048, 080.A-0516, and 082.A-0526).

† E-mail: Luc.Dessart@oca.eu

understand events that are expected theoretically to depend strongly on metallicity. A striking illustration is the case of long-duration γ-ray bursts (GRBs), which are interpreted as stemming from massive stars that avoid angular-momentum depletion through a metallicity-inhibited stellar wind (Woosley 1993; Fruchter et al. 2006).

In distant astrophysical plasmas, the environmental metallicity is typically inferred through the analysis of emission lines produced in photoionized nebulae (Osterbrock 1989). While a variety of techniques are used within this approach, they tend to be limited to oxygen abundance determinations (Kewley & Dopita 2002; Pettini & Pagel 2004) and subject to sizable systematic errors (Kewley & Ellison 2008). Other metal abundances, however, may not scale linearly with that of oxygen. It is well known, for example, that oxygen is primarily produced by massive star explosions (Woosley & Weaver 1995; Arnett 1996), while Type Ia SN (SN Ia) are the main contributors of iron-group elements in the Universe. Hence, an interesting abundance ratio to seek is O/Fe to constrain their relative contributions through the ages.

Furthermore, nebular-line analyses can only be done in environments where the gas density is high enough to produce detectable emission lines. Star clusters in which the gas density is low, either intrinsically or following, for example, the action of massive star winds, cannot be studied for their metallicity this way. When applied to distant galaxies, this method suffers from irrevocable limitations in angular resolution, yielding a metallicity averaged over an extended region rather than the metallicity of a spatially restricted region.[1] This is problematic for determining the metallicity at core-collapse SN sites (Anderson et al. 2010; Stoll et al. 2013), and in particular to quantify the metallicity bias between standard SNe Ib/c sites and those of GRB/SNe (Modjaz et al. 2008, 2011; Sanders et al. 2012).

Modelling stellar spectra offers an alternative to nebular analyses. Quantitative spectroscopy of optical and/or near-IR observations are used to determine the metal abundances in the star's atmosphere. The advantage is that the theory of stellar atmospheres is well developed and accurate enough for abundance determinations (see, e.g., Kudritzki et al. 2012). The drawback is that stars are hard to observe beyond the Local Group, limiting their use to the very nearby Universe.

In this paper, we present an attractive method for metallicity determination that is based on SNe II-Plateau (II-P), which result from the core collapse and subsequent explosion of red supergiant (RSG) stars (Grassberg, Imshennik & Nadyozhin 1971; Van Dyk, Li & Filippenko 2003; Smartt et al. 2004). With such ejecta, it is possible to overcome some of the limitations described above.

(i) SNe II-P are very luminous and thus can be seen out to very large distances; in the phase when the ejecta is optically thick, which lasts for $\sim$100 d after explosion, a standard SN II-P has a typical bolometric luminosity of a few times 10^8 $L_\odot$. Although they are yet to be discovered (and proven to exist), SNe II-P resulting from the pair-production instability are predicted to have even larger plateau luminosities (Kasen, Woosley & Heger 2011; Dessart et al. 2013a), hence, even more attractive detection limits for transient surveys. Over much of this high-luminosity phase, their photosphere is at the hydrogen recombination temperature, i.e. $\sim$7000 K. Consequently, the bulk of this SN II-P radiation emerges in the optical. It is thus particularly suited for observation of nearby and more distant events with optical and near-IR instruments on (very/extremely) large telescopes.

(ii) Of all SNe, only SNe II-P are characterized by photospheres weakly affected by either steady-state or explosive nuclear burning. Specifically, elements beyond O (with the possible exception of Na) are unaffected by steady-state nuclear processing. While chemical mixing may influence the inner parts of the hydrogen-rich envelope of the progenitor RSG stars, the outer parts of the ejecta, which are probed by the photosphere for up to $\sim$80 d after explosion (see, e.g., fig. 5 in Dessart & Hillier 2011), are essentially at the composition of the molecular cloud in which the progenitor star formed.

(iii) Photospheric phase SNe II-P spectra can be modelled with high fidelity using non-local thermodynamic equilibrium radiative-transfer codes like CMFGEN (Dessart & Hillier 2005, 2008; Hillier & Dessart 2012; Dessart et al. 2013b) or PHOENIX (Baron, Branch & Hauschildt 2007). Hence, quantitative spectroscopy can constrain the chemical composition at the photosphere, as routinely done for stellar atmospheres (see, e.g., Hillier & Miller 1998, 1999).

(iv) SNe II-P exhibit spectral signatures associated with a variety of species, including intermediate-mass and iron-group elements. For example, during the recombination epoch, SNe II-P show strong lines of H I, O I, Na I, Ca II, Sc II, Ti II, and Fe II (given in order of increasing atomic mass) – this is a more diverse and eclectic set than the [O III] 5007 Å and [N II] 6584 Å lines seen in H II regions and used for oxygen abundance determinations. As we demonstrate in this paper, metallicity variations in the primordial composition lead to distinct line strengths in the SN II-P optical spectrum as long as the SN photosphere probes the outer progenitor envelope. Hence, in addition to oxygen, one can use a SN II-P spectrum to constrain the mass fractions of additional species, including iron.

The dependence of SN II-P spectra on metallicity variations has been discussed at a qualitative level in the past for standard RSG star explosions (Baron et al. 2003; Dessart & Hillier 2005; Kasen & Woosley 2009; Dessart et al. 2013b), as well as for pair-instability SNe (Kasen et al. 2011; Dessart et al. 2013a). In this work, we use the radiative-transfer simulations of Dessart et al. (2013b) to quantify the sensitivity of a variety of SN II-P spectral signatures to metallicity variations, and investigate whether these variations are sufficiently strong and well behaved to allow the inference of composition. As this study is only meant as a proof of principle, we limit the present discussion to the restricted set of SN II-P models presented in Dessart et al. (2013b), which correspond to the explosion of a massive star evolved from a 15 $M_\odot$ main-sequence star with MESA (Paxton et al. 2011, 2013) at four different metallicities (one-tenth solar, two-fifth solar, solar, and twice solar). In a future study, we will cover a broader range of progenitor and explosion properties, as well as metallicity values.

In the next section, we present the subset of models from Dessart et al. (2013b) that we use in this work. We assess the sensitivity of synthetic spectra to metallicity variations in Section 3 and present a preliminary comparison to observations in Section 4. In Section 5, we present our conclusions and discuss some interesting implications, in particular the prospect of observing SNe II-P with very large and extremely large telescopes to constrain the composition of the Universe out to cosmological distances.

2 SUMMARY OF NUMERICAL SETUP

The simulations we discuss in this work have been presented in Dessart et al. (2013b). For completeness, we summarize the numerical procedure for our calculations.

[1] This limitation can be somewhat overcome for reasonably nearby SNe by using integral field spectroscopy (see, e.g., Rigault et al. 2013).

Table 1. Summary of model properties used as initial conditions for CMFGEN simulations. The first set of models are for different metallicities. The second set includes solar metallicity models evolved with different values of the mixing-length parameter (models m15mlt2, also referred to as mlt2, and m15z2m2 are the same). This second set is used merely to estimate systematic errors in Section 3.

Model	Z ($Z_\odot$)	$M_{\rm final}$ ($M_\odot$)	Age (Myr)	$T_{\rm eff}$ (K)	R_* ($R_\odot$)	L_* ($L_\odot$)	$M_{\rm H}$ ($M_\odot$)	$M_{\rm He}$ ($M_\odot$)	$M_{\rm O}$ ($M_\odot$)	$M_{r,Y_{\rm e}}$ ($M_\odot$)	$M_{r,{\rm H}}$ ($M_\odot$)	$M_{\rm H,\,env}$ ($M_\odot$)	$M_{\rm ej}$ ($M_\odot$)	$E_{\rm kin}$ (B)	$M_{^{56}{\rm Ni}}$ ($M_\odot$)
m15z2m3	0.1	14.92	13.57	4144	524	72 890	7.483	5.048	0.507	1.61	4.15	10.77	13.29	1.35	0.081
m15z8m3	0.4	14.76	13.34	3813	611	71 052	7.183	5.252	0.428	1.63	4.09	10.67	13.12	1.27	0.036
m15z2m2	1.0	14.09	12.39	3303	768	63 141	6.630	5.105	0.325	1.62	3.88	10.21	12.48	1.27	0.050
m15z4m2	2.0	12.60	10.88	3137	804	56 412	5.119	5.042	0.387	1.40	3.77	8.83	11.12	1.24	0.095
m15mlt1	1.0	14.01	12.36	3318	1107	106 958	6.516	5.167	0.354	1.36	3.89	10.13	12.57	1.24	0.121
m15mlt2	1.0	14.09	12.39	3303	768	63 141	6.630	5.105	0.325	1.62	3.88	10.21	12.48	1.27	0.050
m15mlt3	1.0	14.08	12.41	4106	501	64 218	6.542	5.173	0.383	1.54	3.92	10.16	12.52	1.34	0.086

Notes. For the solar composition, we adopt the values of Grevesse & Sauval (1998) and scale each metal mass fraction as indicated. Following the columns containing the cumulative ejecta masses in H, He, and O, we give the Lagrangian mass corresponding to specific locations in the pre-SN star. We give $M_{r,Y_{\rm e}}$, which corresponds to the edge of the iron core, i.e. where the electron fraction $Y_{\rm e}$ rises to 0.49 as we progress outwards from the star centre (this is also the piston location for the explosion) and $M_{r,{\rm H}}$ which corresponds to the base of the H-rich envelope (i.e. the helium-core mass). The last three columns give some ejecta properties that result from the imposed explosion parameters. The quoted ^{56}Ni mass corresponds to that originally produced in the explosion.

Using MESA STAR, Dessart et al. (2013b) generated a grid of models starting with the same main-sequence mass of 15 $M_\odot$ but varying a number of parameters known to influence stellar evolution. In this paper, we focus on the influence of metallicity variations and present results for cases of 0.002, 0.008, 0.02 (taken as our solar metallicity), and 0.04 (named m15z2m3, m15z8m3, m15z2m2, and m15z4m2). When varying the metallicity, we merely scale the mass fraction of each metal by a factor of 1/10, 2/5, 1, and 2. The MESA STAR simulations are performed adopting zero rotation, a mixing-length parameter $\alpha = 1.6$ (we adopt the Schwarschild criterion for convection), a standard resolution (MESH_DELTA_COEFF=1), no core-overshooting, the mass-loss rate recipes dubbed 'Dutch' with a scaling of 0.8 (Table 1). At the end of its life, the solar metallicity model m15z2m2 is a 14.09 $M_\odot$ RSG star with a luminosity of 63141 $L_\odot$, a radius of 768 $R_\odot$, and an effective temperature of 3303 K. It possesses an H-rich envelope of 10.21 $M_\odot$ and a helium core of 3.88 $M_\odot$ (set equal to the Lagrangian mass at the inner edge of the H-rich envelope). The outer edge of the iron core is at a Lagrangian mass of 1.6 $M_\odot$.

Because of the adopted metallicity dependence of RSG mass-loss rates, our MESA STAR models m15z2m3, m15z8m3, m15z2m2, and m15z4m2 have a final H-rich envelope mass that depends on Z, ranging from 10.77 (m15z2m3) down to 8.83 $M_\odot$ (m15z4m2). The efficiency of convective energy transport being set in all four simulations through a mixing-length parameter of 1.6, the variation in metallicity, which changes the opacity in the envelope, alters the stellar radius (since the energy flux to transport from the edge of the core to the stellar surface is essentially the same between these four models). Consequently, for smaller metallicities (opacities), we obtain smaller RSG radii, with values between 524 (m15z2m3) and 804 $R_\odot$ (m15z4m2). Our RSG models are thus both more massive and more compact at lower metallicities. It is important to note that all our models encounter core collapse in the RSG phase. Hence, at least from a theoretical standpoint, there is no reason to believe that 15 $M_\odot$ stars would not yield SNe II-P over a large range of metallicities.

When a mass cell within the iron core reaches an infall velocity of 100 km s^{-1}, each MESA STAR simulation is stopped and a piston-driven explosion is simulated with the grey radiation-hydrodynamics code V1D (Livne 1993). Following the procedure outlined in Dessart, Livne & Waldman (2010), the piston deposits an energy equal to the binding energy of the envelope plus the asymptotic kinetic energy at infinity, which we select to be 1.2 B. V1D treats explosive nucleosynthesis so the change in composition following shock passage is computed. In piston-driven explosions, the amount of ^{56}Ni produced depends sensitively on the adopted location of the piston and the time-scale over which it injects energy. For the current set of simulations, the piston was placed at the base of the Si-rich shell and was given a constant velocity of 10 000 km s^{-1} until the desired energy was reached. In this artificial approach, ^{56}Ni is only produced in the densest (i.e. innermost) ejecta regions crossed by the piston. It is thus essential to apply an artificial mixing to these 1D simulations in order to mimic the mixing that takes place in more realistic multidimensional simulations of core-collapse SNe (Hammer, Janka & Müller 2010).

The mixing we apply is moderate. For example, the initial mass fraction of ^{56}Ni in the four ejecta modelled here is $\sim 10^{-6}$ at 2500 km s^{-1} (a location reached by the photosphere at $\sim$100 d after explosion; see also fig. 5 of Dessart & Hillier 2011). Hence, in our models, radioactive decay has a negligible influence on the SN II-P radiation for most of the plateau length, either through heating, non-thermal ionization/excitation, or abundance variations. In nature, mixing may be stronger and may influence the radiation early on. To ensure we probe only the initial star metallicity, it will be necessary to focus on the mid-plateau phase. In higher energy SN II-P explosions, more ^{56}Ni may be produced and the plateau may be shorter and/or slanted (see section 9 of Dessart et al. 2013b). It is preferable to focus on standard energy explosions, with properties comparable to those of, e.g., SN 1999em.

About 10 d after shock breakout, homologous expansion is reached. The full ejecta is remapped into CMFGEN and evolved until nebular times. A summary of pre-SN and ejecta properties as well as model light curves are given in Dessart et al. (2013b). These four ejecta have a similar colour evolution, plateau length, etc. but they show striking differences in spectral lines, which appear to reflect the variation in the metallicity of their progenitors. The focus of our present study is to discuss these metallicity signatures.

3 SYNTHETIC SIGNATURES OF METALLICITY VARIATIONS IN SNe II-P

Discussing spectroscopic differences within a set of SN II-P models is complicated by the potentially distinct rates of evolution of their colour and ejecta ionization. To disentangle abundance and ionization effects, which are both known to alter line strengths, it is best to compare these SN II-P models during the photospheric phase and

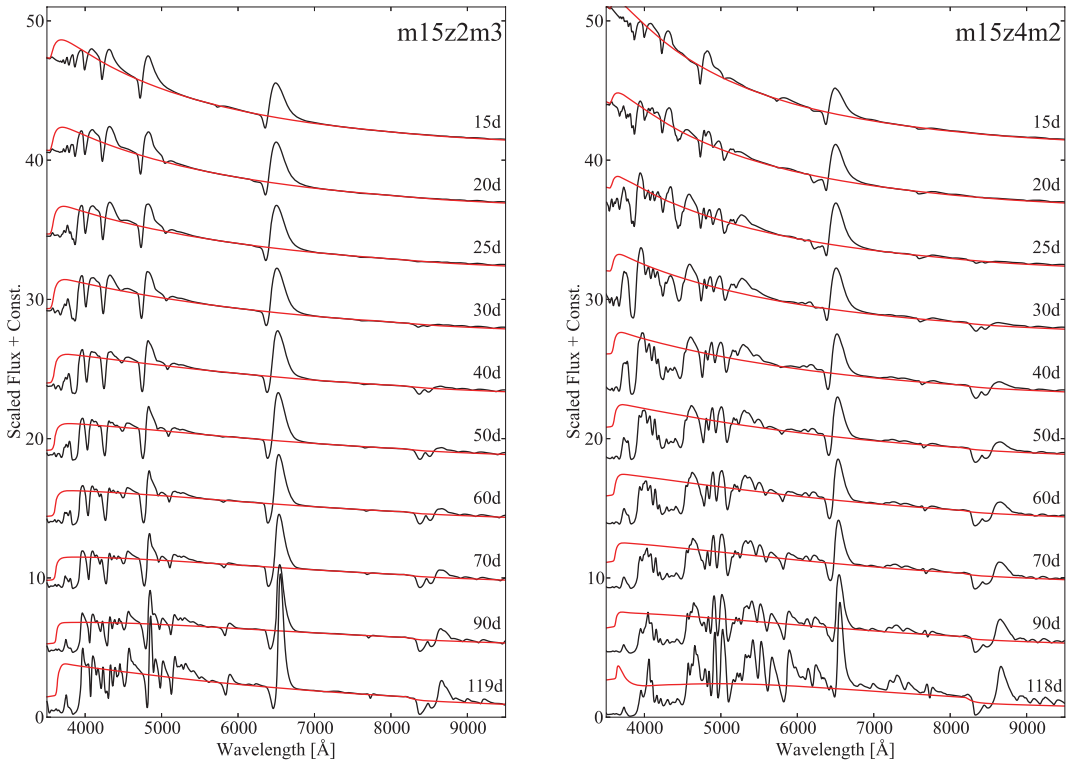

Figure 1. Spectral evolution in the optical range for SN II-P models at one-tenth (m15z2m3, left) and twice (m15z4m2, right) the solar metallicity, highlighting their sensitivity to metallicity variations. The UV range is also sensitive to metallicity variations but lines tend to overlap and to be saturated, which complicates the analysis. The red curve corresponds to the synthetic continuum flux. Line identifications are discussed in detail in the appendix of Dessart et al. (2013b).

when they have the same colour, as done in Dessart et al. (2013b) at $U - V$ of -0.4, 0.4, and 1.7 mag. Despite the comparable spectral energy distributions at a given colour, our set of SN II-P models shows considerable diversity in individual lines strengths, and in particular during the recombination phase when metal-line blanketing strengthens. This phase typically starts a month after explosion, although variations in progenitor radius can delay its onset (Dessart et al. 2013b). The lower the metallicity, the weaker the metal lines appear (Fig. 1). The most obvious variations are in the following spectral lines or groups of lines (given in order of increasing atomic mass of the parent species):

(i) O I 7777 Å,
(ii) Na I D,
(iii) the Ca II triplet at 8500 Å and the semi-forbidden-line doublet at 7300 Å,
(iv) the Ti II broad blanketing region ranging from 4200 to 4500 Å, and associated with the atomic configurations $3d^24s$–$3d^24p$, $3d^3$–$3d^24p$,
(v) Sc II 5239 Å ($4s^2\ ^1Se$–$4p\ ^1Po$), 5526 Å ($3d^2\ ^1Ge$–$4p\ ^1Fo$), 5669 Å ($3d^2\ ^1GPe$–$4p\ ^3Po$), and companion configurations,
(vi) Fe II 4923, 5018, and 5169 Å ($3d^54s^2Se$–$3d^6$ 4p Po terms).

Because of line overlap, numerous other lines, from these or other metal species, prevent a clear connection to a metallicity variation, particularly when the metallicity is super-solar (model m15z4m2). In this case, the total flux (black curve) departs significantly from the continuum flux level (red curve), even between neighbouring P-Cygni profiles. In contrast, even when metal-line blanketing is strong, the lower metallicity model m15z2m3 still exhibits well-isolated P-Cygni profiles, with the flux going back to the continuum level in-between neighbouring features.

The UV range is very sensitive to the metal composition at the photosphere. Indeed, it is strongly attenuated by metal-line blanketing, even at one-tenth solar metallicity. Numerous metal lines overlap and may remain saturated even when the metal abundance decreases. Bumps and valleys in the UV range do not correspond to specific line features, but reflect absorption variations instead. So, bumps are merely regions of reduced absorptions (i.e. not residual emission above the continuum level). Hence, one cannot in general associate a given feature with a specific metal line, complicating the inference of metal abundances from UV spectra. The UV flux is also faint because of the low temperature of the photosphere during the recombination epoch. Hence, the UV domain is not ideal if we wish to determine robust metallicity signatures from SNe II-P spectra over a large range of distances.

The strong differences shown in Fig. 1 can be quantified by means of line-absorption equivalent widths (EWs), which we measure for each time step in each model sequence. With CMFGEN, we can compute the continuum flux for each epoch and thus calculate the true EW for any feature. However, line overlap often prevents the association of a given feature with a given transition in a given atom/ion. To identify an abundance effect on specific lines, which is our first goal, we compute the spectrum for each species individually. Doing these EW calculations on theoretical models is automatic and unambiguous, which is why in this model section we show such measurements, as opposed to the standard pseudo-EW (pEW) extracted from observed spectra. We show the results of true EW calculations on Hα, O I 7777 Å, Na I D, Fe II 5018 Å, Fe II 5169 Å, and Ca II 7300 Å in Fig. 2.

The Hα EW becomes more and more negative as the SN model proceeds through the photospheric phase. This is not a signature of an abundance variation but simply a reflection of the changing

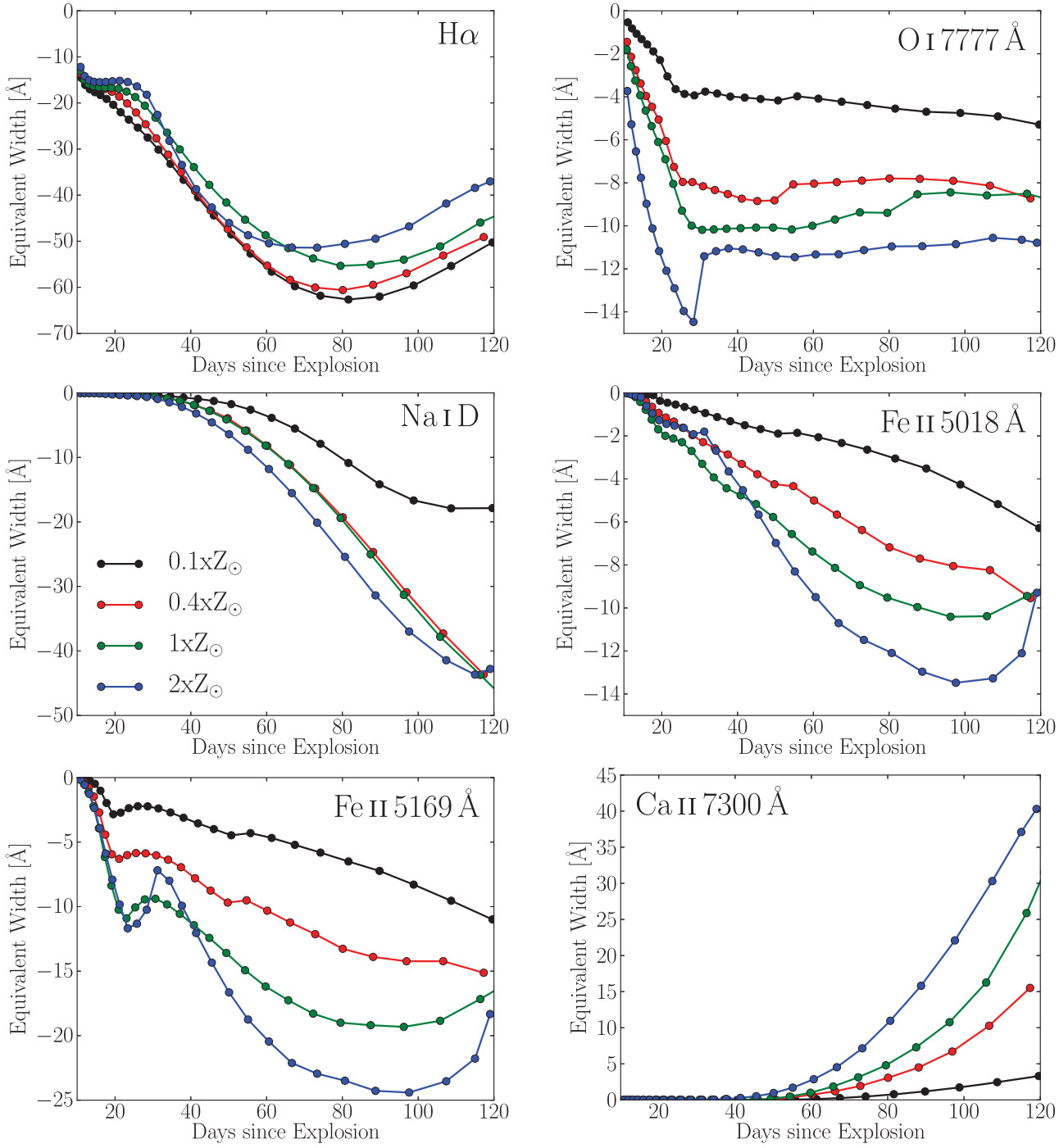

Figure 2. First five panels from top left: evolution of the line-absorption EW associated with Hα (top left), O I 7777 Å (top right), Na I D (middle left), Fe II 5018 Å (middle right), and Fe II 5169 Å (bottom left). Bottom-right panel: evolution of the EW for the pure emission feature associated with the Ca II 7300 Å doublet. Each coloured curve corresponds to a different ejecta model resulting from the explosion of a 15 $M_{\odot}$ star evolved at a different metallicity (see Section 2 for details).

density and temperature conditions in the spectrum formation region (Dessart & Hillier 2011; Dessart et al. 2013b), as well as the increasing importance of time-dependent effects on the ionization (Utrobin & Chugai 2005; Dessart & Hillier 2008). The small differences in Hα EW among sequences are caused by small variations in blanketing of the UV flux. This affects the radiation through the photosphere and the formation of Hα, but the change in metallicity leaves the H mass fraction basically untouched.

A much stronger trend of increasing absorption/emission is present for lines associated with underabundant species (Fig. 2). The magnitude of the effect varies considerably from low to high metallicity, which is not surprising since metallicity variations yield significant changes in the associated species mass fraction. The evolution of the EW can be non-monotonic, and its magnitude may behave non-linearly with metallicity. If we select mid-plateau epochs (∼50 d after explosion), we see that the O and Fe line strengths

reflect with fidelity the variations in metallicity. The effect is strong – between models m15z2m3 and m15z4m2, the EW of O I 7777 Å and Fe II 5018 Å or Fe II 5169 Å varies by a factor of 3–4.

The Ca II semi-forbidden lines at 7300 Å, which are optically thin and in emission, also show a strong sensitivity to metallicity. These lines are observed and predicted here in our models during the second half of the plateau phase, hence, well before the nebular phase. The associated line emission takes place in the outer SN ejecta (the former H-rich envelope) whose density is much lower than that of the inner ejecta at those epochs. In the SN context, the ejecta temperature and electron density are well constrained by the model and are comparable for the four models discussed here. Thus, the differing line strengths stem exclusively from variations in the Ca abundance in the H-rich envelope and hence offer an additional probe of the metallicity. The differences between models are huge (i.e. a factor of 10 between models m15z2m3 and m15z4m2). An important signature is that the model with a metallicity of one-tenth solar shows negligible Ca II 7300 Å emission during the photospheric phase.

While there is no sizable error on the EW measurements performed on synthetic spectra, there are systematic errors associated with the modelling and these are hard to estimate. A lot of work has been devoted to test the code and ensure that the results are as accurate as possible. We use a set of large model atoms, in particular for Fe I and Fe II, because it is essential at the recombination epoch to obtain accurate colours (Dessart et al. 2013b). In our simulations, doubling the spatial or frequency resolution does not change the synthetic spectra. The results are apparently well converged in a numerical sense.

The main source of error in assessing metallicities from synthetic spectra will likely come from using ejecta or progenitor star models that are not suitable for the observed SN under consideration. For example, progenitor stars of different surface radii at the time of explosion produce SNe II-P that follow a different colour evolution, exhibiting a significant variation in the time at which recombination occurs. Dessart et al. (2013b) explored this issue by means of physical stellar evolution models (at solar metallicity) in which the mixing-length describing convection was modified from the standard value of 1.6 (model mlt2; $R_* = 768\ \mathrm{R}_\odot$) to 1 (model mlt1; $R_* = 1107\ \mathrm{R}_\odot$) and 3 (model mlt3; $R_* = 501\ \mathrm{R}_\odot$). Only the model mlt3 fitted the observations of SN1999em, implying that the stellar radius is not a free parameter but is instead constrained from observations – the other models remained too blue for too long. In Fig. 3, we show the evolution of the EW in Fe II 5169 Å for these three models. The different times for the onset of recombination is evident; the models that recombine first (more compact progenitor), also show the strongest EW at the recombination epoch. The differences here are tied to the progenitor radius, while the metallicity, being solar for all three models, plays no role. This illustration gives some measure of the potential errors in our method but it gives a clear overestimate. When modelling an SN, the progenitor radius is one entity that we constrain – it is not a free parameter, and the same holds for the envelope mass or the explosion energy. Hence, it is important to select carefully the SN II-P we employ for metallicity determinations. As we discuss below, it is critical to exclude from this study all SNe II-P with a significant slant in *V*-band light curve during the photospheric phase, because unlike our present models they are not genuine plateau SNe. Furthermore, in this study, we must select observations that are roughly compatible with our four models m15z2m3, m15z8m3, m15z2m2, and m15z4m2 (similar kinetic energy, similar colour evolution). In the future, we will need to produce tailored models for each observed SN under study in order to limit potential systematic errors.

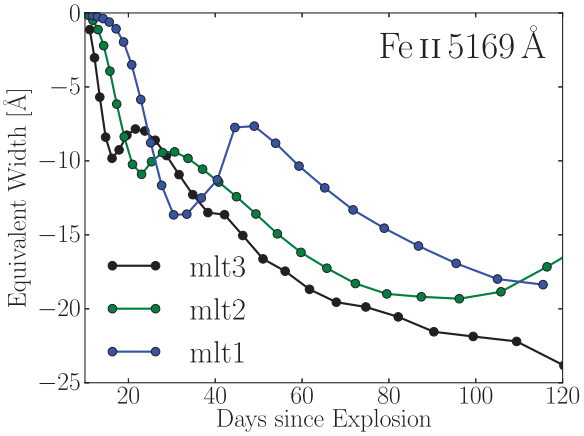

Figure 3. Evolution of the EW in Fe II 5169 Å for solar metallicity models m15mlt1, m15mlt2, m15mlt3 (labels omit 'm15' since redundant). Here, the distinct tracks stem from the variation in progenitor radius for the three progenitor star models. To reduce systematic errors when inferring metallicities, it is important to employ an SN II-P model that corresponds closely to the SN under study.

4 COMPARISON TO OBSERVATIONS

Measuring EWs in observed spectra can be difficult. If we have a radiative-transfer model that matches the observed SN flux we can also compute the continuum flux and proceed with the rectification of the spectrum. Lacking a model, the evaluation of the continuum level can be very uncertain, in particular shortward of ∼5000 Å during the recombination phase. In this case, it is customary to measure pEWs, by calculating the area in absorption bounded by the local flux maxima around a given line-absorption feature. Such measurements are typically done on features for which one transition is expected to dominate the absorption, e.g. Fe II 5169 Å. In reality, this assumption is not guaranteed and the value of such a measurement may be difficult to interpret.

Although more straightforward than measuring true EWs, measuring pEWs can still be problematic when line blanketing and overlap are strong, as in model m15z4m2 (Fig. 1). For Hα, the presence of overlapping lines of Si II early on and Fe II at the recombination epoch introduces some ambiguity in the measurement. The broad Ti II blanketing region is much worse in that respect although it is clear that the associated absorption is strongly sensitive to metallicity in our models (see also Dessart et al. 2013b). For iron, rather than using the strong Fe II 5169 Å, which shows signs of overlap, it is more convenient to use Fe II 5018 Å; it is bounded by two Fe II lines that make the Fe II 5018 Å absorption dip easy to measure.

For this work, we use the data base of SNe II from the Carnegie SN Project (CSP; Hamuy et al. 2006) and other followup programmes: the Calan/Tololo SN Survey (Hamuy et al. 1993), the Cerro Tololo SN programme, the SN Optical and Infrared Survey (Hamuy et al. 2002) and the Carnegie Type II SN Survey (Hamuy et al. 2009). Anderson et al. (2014) have studied their *V*-band light curves to reveal the diversity in fading rate through the plateau phase, and thus the presence of intermediate events between plateau and linear SNe II. Here, we select events that show a rough photometric and spectroscopic compatibility with our four basic SNe II-P models. In practice, we exclude SNe that show an appreciable slant in the *V*-band light curve (events with an $s2 > 1$; see Anderson et al. 2014 for details). We also exclude events that have a strongly delayed onset of the recombination phase (suggesting an anomalously slow ejecta cooling, as may arise from a progenitor envelope that is

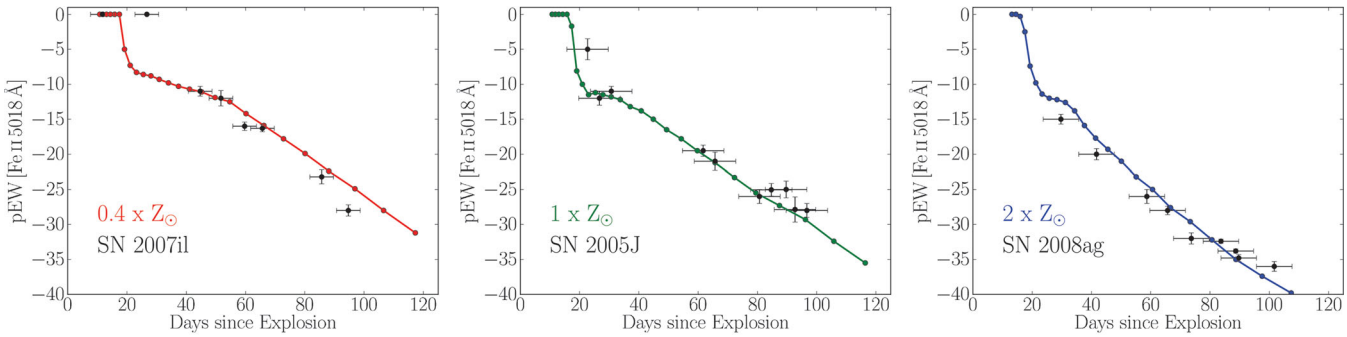

Figure 4. Comparison of pEWs between observations (SNe 2007il, 2005J, and 2008ag) and SN II-P models of increasing metallicity (0.4, 1, 2 times solar from left to right). The same measurement procedure is used on observed and synthetic spectra.

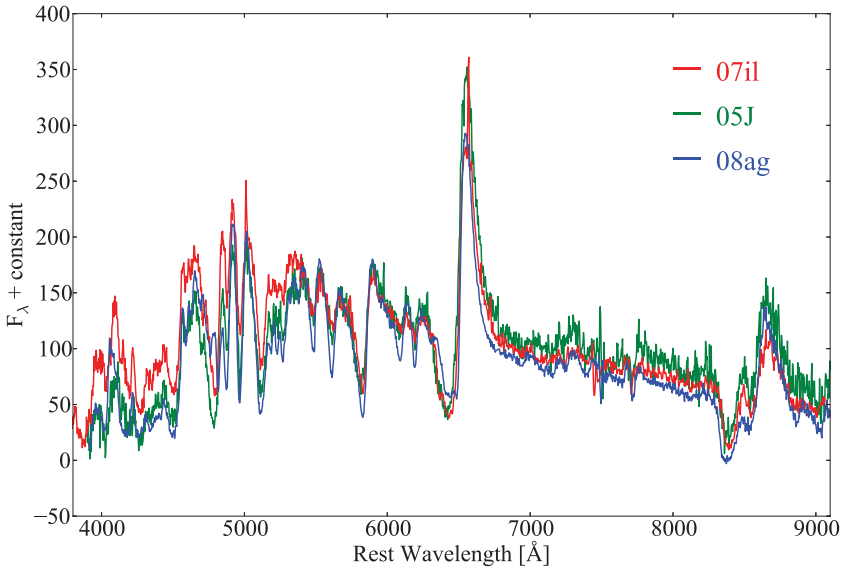

Figure 5. Montage of spectra for the three SNe II-P shown in Fig. 4. The time is ∼80 d after explosion.

more extended that normal, e.g. SN 2004er; Modjaz et al. 2004; Anderson et al. 2014). This rough filtering is necessary in order to isolate spectral diversity associated with variations in primordial composition rather than with SN energetics or progenitor structure (even if there may well be a connection between these various progenitor/explosion properties). Doing this filtering is essential to reduce systematic errors. In the future, we will need to use a broader sample of progenitor/explosion models at different metallicity to reflect the SN II diversity or produce a tailored model for each SN under study.

In Fig. 4, we first show the pEW of Fe II 5018 Å for three SNe II-P. The errors for each data point include one on the explosion time. We may set it equal to the time between detection and prior non-detection, estimate it using SNID (Blondin & Tonry 2007), or use an inference from SN modelling (e.g. SN 1999em; Dessart & Hillier 2006). The other error is on the pEW, which is estimated from repeating the measurement multiple times. The pEW in Fe II 5018 Å follows quite closely the trajectories of models m15z8m3 (0.4 $Z_\odot$; 2007il), m15z2m2 ($Z_\odot$; 2005J), and m15z4m2 (2.0 $Z_\odot$; 2008ag) – no SN follows the morphology of model m15z2m3 (0.1 $Z_\odot$). Fig. 4 suggests that some observations exhibit relatively weak or strong Fe II lines (Fig. 5) in a systematic fashion, and in that respect reflect our results from sub- to super-solar metallicity models.

When we focus on the recombination phase, around 80 d after explosion, we find that the larger sample of SNe II is well distributed within the tracks of models at 0.4 and 2 $Z_\odot$ (Fig. 6). There is a marked scarcity of SNe II-P at metallicity below that found in the large magellanic cloud. For comparison, we add the location of SN 1999em, which sits at a slightly super-solar metallicity value.

Progenitor metallicities of core-collapse SNe discovered by means of targeted surveys have been studied in the past by Anderson et al. (2010). Using nebular-line analyses of a coincident or nearby H II region, they infer a 12 + log [O/H] of 8.14 for SN 2003E, 8.24 for SN 2002gw, 8.52 for SN 1992ba, 8.73 for SN 2003B, 8.61 for SN 1999em, and 8.64 for SN 2003T (on the N2 scale of Pettini & Pagel 2004). These values reflect within the uncertainties the trend we obtain with our pEW measurements, and thus confirm the results shown in Fig. 6. Anderson et al. (2010) do not find any SN II-P at low metallicity, although this may result from using SNe in high-luminosity hosts, which are biased towards high metallicity. The untargeted survey from the Palomar Transient Factory also have no SN II-P at very low metallicity (Stoll et al. 2013). In the future, we will perform a more complete analysis of both SNe II-P and host galaxies/H II regions to compare in detail the metallicity inferred from both techniques. We will also extend the sample to include SNe II-P from untargeted surveys.

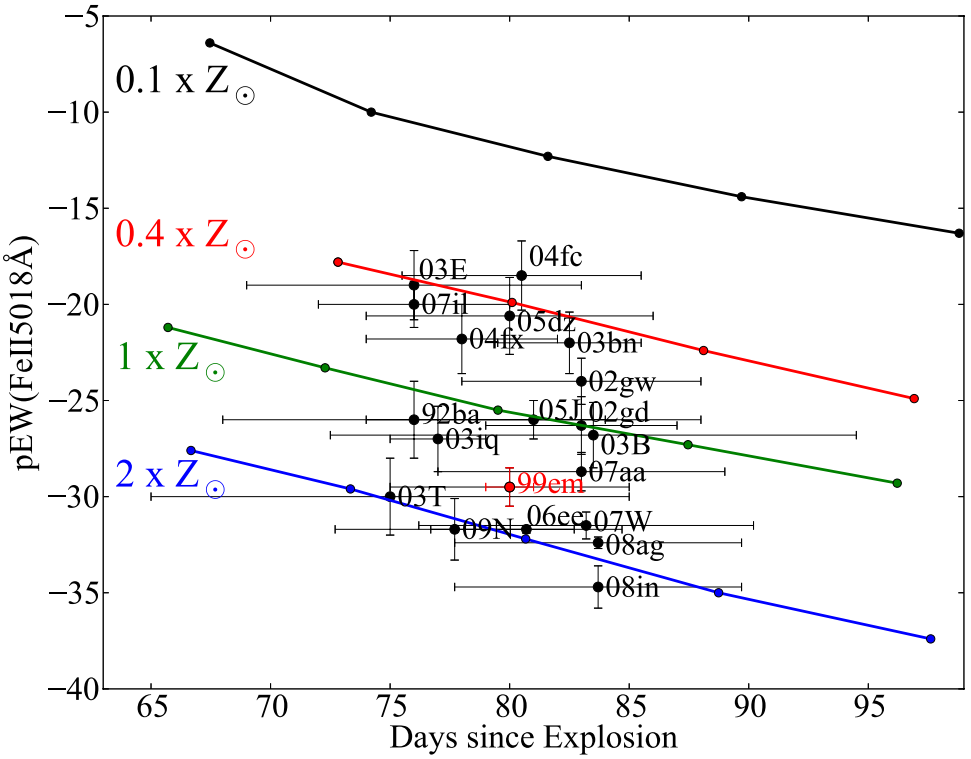

Figure 6. Distribution of data measurements of pEWs for observed SNe II-P and the corresponding tracks of theoretical points for models m15z2m3, m15z8m3, m15z2m2, and m15z4m2 (models at 0.1, 0.4, 1, and 2 $Z_{\odot}$). Note the scarcity of standard SNe II-P in the vicinity of the model at one-tenth solar metallicity. For comparison, we also add the location of SN 1999em in this plane [the explosion time for 1999em was inferred by Dessart & Hillier (2006), with an error of ± 1.0 d].

5 DISCUSSION AND CONCLUSIONS

Extending the previous parameter study of Dessart et al. (2013b), we have explored in more detail the systematic variations of SN II-P spectra with metallicity. Provided one limits the epochs to a few weeks prior to the end of the plateau phase, the metal lines appearing in SN II-P spectra reflect the metallicity of the progenitor star, and allow one to place some constraints on the abundances of oxygen, sodium, titanium, scandium, or iron. This wide range of species spans from moderate to high atomic mass, and is produced by nuclear burning under different conditions (e.g. steady-state burning in stars versus explosive burning in SNe).

In this paper, we have quantified the variations of the line-absorption EW with metallicity in several strong and/or isolated lines including O I 7777 Å, Na I D, Ti II absorption at 4200–4500 Å, Fe II 5018, Fe II 5169 Å, as well as the Ca II 7300 Å emission doublet. More lines could be studied but this diverse set is good for the proof-of-concept discussion. We also avoid using the UV range due to the low fluxes, saturated and badly blended lines, and the sensitivity to parameters other than metallicity. We find that in all models, the evolution through the plateau phase leads to a systematic increase in the magnitude of these EWs. Hα shows little sensitivity to metallicity, while Na I D becomes markedly weaker only when the metallicity is decreased to one-tenth solar. However, O I 7777 Å, Fe II 5169 Å, and Fe II 5018 Å exhibit a systematic trend at all times that correlates with the metallicity of the model. A good time for analysis is during the recombination phase, when metal-line blanketing is strong, but before the end of the plateau to avoid any pollution at the photosphere, as may occur through the mixing of species from the helium core into the H-rich envelope.

We have confronted the models to a selection of SNe II-P from the CSP and former followup programmes (Hamuy et al. 2006; Anderson et al. 2014). Calculating pEWs on both observations and models at the recombination epoch, we find that they exhibit the same behaviour from the early-photospheric phase until the end of the plateau (e.g. increasing EW magnitude in Fe II 5018 Å). Comparing the measurements at $\sim$80 d after explosion, we find that all selected SNe fall within the pEW limits set by the 0.4 and 2 $Z_{\odot}$ models. No SN II-P in our sample matches the weak metal-line strengths of our model at $Z_{\odot}/10$. Since the CSP observations are probably representative of SNe II, we speculate that we are yet to observe an SN II-P at small magellanic cloud metallicity in the local Universe.

Our metallicity measurements compare favourably with nebular-line analyses. Such studies, based on both targeted (Anderson et al. 2010) and untargeted (Stoll et al. 2013) surveys, confirm the scarcity of SNe II-P at low metallicity. The absence of low-metallicity SNe in our sample most likely reflects the paucity of very low metallicity systems in the local universe. The absence of low-metallicity hosts is also seen in the analysis of core collapse SNe out to $z \sim 0.2$ by Kelly et al. (2014). Since stellar evolution depends on metallicity, it is important to study SN at low metallicities. Extreme rotation rates on the main sequence, for example, can prevent a star, if it has an initial mass of $\gtrsim$20 $M_{\odot}$, from evolving to the red and from exploding as an RSG (see, e.g., Brott et al. 2011). Irrespective of rotation, stars in the mass range 10–20 $M_{\odot}$ are expected to explode in an RSG phase at low metallicity and thus should be seen.

In addition to providing important constraints on the SN and its progenitor, quantitative spectroscopy of SNe can also be used for

determining the evolution of metallicity with redshift, and for revealing the metallicity distribution with galactocentric radius. The high luminosity of SNe makes them ideal substitutes to stars (see, e.g., Kudritzki et al. 2012), but may also offer an alternative to nebular-line analyses (Osterbrock 1989; Kewley & Dopita 2002; Pettini & Pagel 2004). At very large distances, we will need super-luminous SNe resulting from the pair-production instability in a super-massive RSG star, since their plateau luminosities are predicted to be of the order of 10^{10} rather than a few 10^8 $L_\odot$ (Kasen et al. 2011; Dessart et al. 2013a). Unfortunately, such super-luminous SN II-P events are yet to be discovered.

With VLT-FORS, an SN II-P of 14th magnitude at 10 Mpc requires a 0.7 s exposure to yield an S/N of 30 per pixel (grism 150I). At 100 Mpc, this exposure time is 70 s. Using a Hubble constant of 70 km s^{-1} Mpc^{-1}, that same SN at a redshift of 0.1 would require an exposure of about 30 min for the same setup. With the future extremely large telescopes, going up to redshift 1 and beyond may be possible. In practice, to reduce systematic errors from the modelling and to circumvent inaccurate pEWs measurements, it will be desirable to perform detailed modelling of each SN II-P under study.

ACKNOWLEDGEMENTS

LD acknowledges financial support from the Unité Mixte Internationale 3386 (Laboratoire Franco-Chilien d'Astronomie, CNRS/INSU France, Universidad de Chile), European Community through the International Re-integration Grant PIRG04-GA-2008-239184, and 'Agence Nationale de la Recherche' through the grant ANR-2011-Blanc-SIMI-5-6-007-01. CPG acknowledges support from CONICYT-AGCI PhD studentship. CPG, MH, JPA, and FL acknowledge support from the Millennium Center for Supernova Science through grant P10064-F and the Millennium Institute for Astrophysics grant IC120009, funded by Programa Iniciativa Cientifica Milenio. DJH acknowledges support from STScI theory grant HST-AR-12640.01 and NASA theory grants NNX10AC80G and NNX14AB41G. This work was granted access to the HPC resources of CINES (France) under the allocation c2013046608 made by GENCI (Grand Equipement National de Calcul Intensif). GF acknowledges financial support by Grant-in-Aid for Scientific Research for Young Scientists (23740175). This material is based upon work supported by NSF under grants AST-0306969, AST-0908886, AST-0607438, and AST-1008343. MS acknowledges the generous support provided by the Danish Agency for Science and Technology and Innovation through a Sapere Aude Level 2 grant.

REFERENCES

Anderson J. P., Covarrubias R. A., James P. A., Hamuy M., Habergham S. M., 2010, MNRAS, 407, 2660
Anderson J. P. et al., 2014, ApJ, submitted
Arnett D., 1996, Supernovae and Nucleosynthesis: An Investigation of the History of Matter from the Big Bang to the Present. Princeton Univ. Press, Princeton, NJ
Baron E., Nugent P. E., Branch D., Hauschildt P. H., Turatto M., Cappellaro E., 2003, ApJ, 586, 1199
Baron E., Branch D., Hauschildt P. H., 2007, ApJ, 662, 1148
Blondin S., Tonry J. L., 2007, ApJ, 666, 1024
Boissier S., Prantzos N., 1999, MNRAS, 307, 857
Brott I. et al., 2011, A&A, 530, A115
Burbidge E. M., Burbidge G. R., Fowler W. A., Hoyle F., 1957, Rev. Mod. Phys., 29, 547
Dessart L., Hillier D. J., 2005, A&A, 437, 667
Dessart L., Hillier D. J., 2006, A&A, 447, 691
Dessart L., Hillier D. J., 2008, MNRAS, 383, 57
Dessart L., Hillier D. J., 2011, MNRAS, 410, 1739
Dessart L., Livne E., Waldman R., 2010, MNRAS, 408, 827
Dessart L., Waldman R., Livne E., Hillier D. J., Blondin S., 2013a, MNRAS, 428, 3227
Dessart L., Hillier D. J., Waldman R., Livne E., 2013b, MNRAS, 433, 1745
Fruchter A. S. et al., 2006, Nature, 441, 463
Grassberg E. K., Imshennik V. S., Nadyozhin D. K., 1971, Ap&SS, 10, 28
Grevesse N., Sauval A. J., 1998, Space Sci. Rev., 85, 161
Hammer N. J., Janka H.-T., Müller E., 2010, ApJ, 714, 1371
Hamuy M. et al., 1993, AJ, 106, 2392
Hamuy M. et al., 2002, AJ, 124, 417
Hamuy M. et al., 2006, PASP, 118, 2
Hamuy M. et al., 2009, ApJ, 703, 1612
Hillier D. J., Dessart L., 2012, MNRAS, 424, 252
Hillier D. J., Miller D. L., 1998, ApJ, 496, 407
Hillier D. J., Miller D. L., 1999, ApJ, 519, 354
Kasen D., Woosley S. E., 2009, ApJ, 703, 2205
Kasen D., Woosley S. E., Heger A., 2011, ApJ, 734, 102
Kelly P. L., Filippenko A. V., Modjaz M., Kocevski D., 2014, preprint (arXiv:1401.0729)
Kewley L. J., Dopita M. A., 2002, ApJS, 142, 35
Kewley L. J., Ellison S. L., 2008, ApJ, 681, 1183
Kudritzki R.-P., Urbaneja M. A., Gazak Z., Bresolin F., Przybilla N., Gieren W., Pietrzyński G., 2012, ApJ, 747, 15
Livne E., 1993, ApJ, 412, 634
Modjaz M., Challis P., Kirshner R., Calkins M., 2004, IAU Circ., 8415, 2
Modjaz M., Kewley L., Bloom J. S., Filippenko A. V., Perley D., Silverman J. M., 2011, ApJ, 731, L4
Modjaz M. et al., 2008, AJ, 135, 1136
Nomoto K., Kobayashi C., Tominaga N., 2013, ARA&A, 51, 457
Osterbrock D. E., 1989, Astrophysics of Gaseous Nebulae and Active Galactic Nuclei. University Science Books, Mill Valley, CA
Paxton B., Bildsten L., Dotter A., Herwig F., Lesaffre P., Timmes F., 2011, ApJS, 192, 3
Paxton B. et al., 2013, ApJS, 208, 4
Pettini M., Pagel B. E. J., 2004, MNRAS, 348, L59
Rigault M. et al., 2013, A&A, 560, A66
Sanders N. E. et al., 2012, ApJ, 758, 132
Smartt S. J., Maund J. R., Hendry M. A., Tout C. A., Gilmore G. F., Mattila S., Benn C. R., 2004, Science, 303, 499
Stoll R., Prieto J. L., Stanek K. Z., Pogge R. W., 2013, ApJ, 773, 12
Tremonti C. A. et al., 2004, ApJ, 613, 898
Utrobin V. P., Chugai N. N., 2005, A&A, 441, 271
Van Dyk S. D., Li W., Filippenko A. V., 2003, PASP, 115, 1289
Woosley S. E., 1993, ApJ, 405, 273
Woosley S. E., Weaver T. A., 1995, ApJS, 101, 181

This paper has been typeset from a TEX/LATEX file prepared by the author.